UWB Tomographic Radar Imaging of Penetrable and Impenetrable Objects

Ultrawide-band tomography, producing images that show slices of objects, is less harmful than x-rays and can provide useful, high resolution images.

By Lluís Jofre, *Senior Member IEEE*, Antoni Broquetas, *Member IEEE*, Jordi Romeu, *Member IEEE*, Sebastián Blanch, *Member IEEE*, Anna Papió Toda, Xavier Fàbregas, *Member IEEE*, and Angel Cardama, *Member IEEE*

ABSTRACT | In this paper, the capability of ultra-wide-band (UWB) sensor arrays for tomographic radar of electrically large objects is presented. The major concern when imaging is extended to real objects is to achieve a correct reconstruction of the object shape and its electric properties. A general framework based on a UWB bifocusing operator (UWB-BF) with good tomographic imaging capabilities is presented. This general approach provides a comprehensive understanding of the basic tradeoffs with regard to sensing geometry and image quality parameters. Through numerical simulations and measurements applied to canonical as well as to complex objects, basic design criteria are assessed and the potential of UWB tomographic radar imaging is presented.

KEYWORDS | Microwave imaging; radar imaging; sensing arrays; tomography; ultra-wide-band (UWB)

I. INTRODUCTION

The capability of microwave signals to penetrate light opaque materials and sense distant or inaccessible objects with reasonable spatial resolution makes them attractive for different industrial, medical, civil, and security applications [1]–[9]. Wide-band signals such as those produced with ultra-wide-band (UWB) systems [10], [11], and in particular the recent 3.1–10.6 GHz band, offer new possibilities to increase spatial resolution and dielectric parameter measurement accuracy.

The existing tomographic radar imaging systems rely basically on two main techniques: those based on radar techniques [12]–[21], aimed at the location of specific scatterers inside the test area, and those aimed at the reconstruction of the internal parameters of the objects, normally based on tomographic approaches [22]–[30]. Although hybrid approaches exist, a general trend is that radar-based techniques are time domain. They use computationally efficient synthetic aperture radar (SAR) algorithms and provide accurate object shape and location results. Instead, tomography-based techniques tend to be frequency domain and to use different forms of back-projection algorithms. They are progressively based on nonlinear iterative inversion algorithms [31], [32] and give accurate information on the dielectric properties of the objects for moderate size-contrast products. When the interest is the tomographic reconstruction of high-contrast electrically extended objects, the inversion problem becomes highly nonlinear and the existing techniques suffer from a lack of accuracy (ill-conditioned matrices) or low computational efficiency (time-expensive inversion or iterative methods). Consequently, new imaging approaches are needed. Most of the imaging methods, either mono- or multifrequency, are strongly dependent on the frequency or set of frequencies used in the measurement. Regardless of the frequency behavior of the constituent parameters of the object under test, the interaction of the illuminating fields with the object is highly frequency

dependent and prone to excite resonances. As a result, the reconstructed images are heavily sensitive to the operating frequency band. Instead, when a continuous frequency spectrum or, equivalently, a very short temporal impulse is employed for the exploration, a reduction of the resonant character of the reconstruction is observed. In this sense UWB tomographic radar imaging provides clear advantages compared to its mono- or multifrequency alternatives, in addition to obvious superior performance in terms of higher resolution.

The aim of this paper is to present a UWB focusing operator for arbitrary short-range encircling geometries and to analyze its robustness for different kinds of impenetrable and penetrable objects in terms of frequency bandwidth and permittivity dispersion, electric contrast, and geometrical configuration. This paper intends to provide clear guideline to determine tomographic radar imaging system parameters and specifications.

This paper is organized as follows. In Section II, the UWB bifocusing (UWB-BF) algorithm is introduced and its general properties discussed. Also the minimum space, frequency, and time sampling criteria are reviewed in terms of the dimension of the reconstruction area and practical measurement aspects. In Section III, the general formulation is applied to the reconstruction of the shape of a complex impenetrable object illustrating the high spatial resolution capabilities of the UWB. In Section IV, tomographic imaging of penetrable objects is discussed, with special emphasis on the effects on the quality of the image for high contrasted objects as a function of the number and placement of sensors. Section V is devoted to conclusions.

II. UWB TOMOGRAPHIC RADAR SENSING AND IMAGING

The general idea for UWB tomographic radar imaging consists of distributing a certain number of microwave sensors (transmitters and/or receivers) on a certain region, surrounding as much as possible the object under investigation, as shown in Fig. 1). The goal is to obtain the spatial and electrical information of the extended object $\varepsilon_t(\vec{r})$ relative to the original background constant

Fig. 1. *Sensing geometry.*

value ε_b of the interrogation area S_0. The object can be a continuous distribution or a discrete set of objects S_k with electrical permittivity $\varepsilon_{S_k}(\vec{r})$. Because the electric parameters of both the object and the background medium may have certain frequency dependence, its possible impact on the resulting image must be studied. In this paper, relative object permittivity variations up to 40% along the operating bandwidth have been simulated, showing little impact on the resulting images.

The presented formulation and images correspond to a two-dimensional (2-D) geometry, which can be extended to the three-dimensional (3-D) case using the appropriate Green function.

A. UWB-BF Analytical Formulation

In the 2-D geometry, the object is assumed invariant in the z-axis. This allows a scalar formulation of currents and electric fields parallel to the z-axis. A 2-D geometry is applicable to tomographic systems able to focus the illumination in a layer of the explored body. Following the electromagnetic compensation principle [33], the illumination by a transmitter located at $\vec{r}_{T_i}$ at a frequency f of an object by a field $E(\vec{r}, f; \vec{r}_{T_i})$ induces an equivalent electric current distribution proportional to the electrical contrast $c(\vec{r}) = (\varepsilon_t(\vec{r}) - \varepsilon_b)/\varepsilon_b$ defined as

$$J_{eq}(\vec{r}, f; \vec{r}_{T_i}) = j\omega\varepsilon_b c(\vec{r}) E(\vec{r}, f; \vec{r}_{T_i}). \tag{1}$$

The induced current at every point of the object as seen in (1) depends for every frequency on both the local contrast value and the value of the illuminating field created by the particular transmitter being active at that moment. This current may be seen as the source of the scattered field in the sensing process and as an illumination-dependent "trace" of the original object.

As shown in Fig. 1, a set of N_T transmitters (T_i) and a set of N_R receivers (R_j) are used to scan the interrogation area where the reconstruction algorithm is applied. First, a measurement matrix (information matrix) is obtained as follows: for every frequency and transmitting element, the scattered field is measured over each receiving element, obtaining an N_R measurement vector. Then the procedure is repeated for the N_T transmitting elements obtaining an $N_T \times N_R$ matrix. For a monostatic setup $N_R = 1$ and the matrix becomes a vector.

The scattered field measured at a receiver positioned at $\vec{r}_{R_j}$ created by the equivalent current $J_{eq}(\vec{r}, f; \vec{r}_{T_i})$ may be expressed as

$$E_s\left(\vec{r}_{R_j}, f; \vec{r}_{T_i}\right) = -j\omega\mu_0 \int_{V_0} J_{eq}(\vec{r}, f; \vec{r}_{T_i}) . G\left(\left|\vec{r}_{R_j} - \vec{r}\right|, f\right) dV$$

$$\tag{2}$$
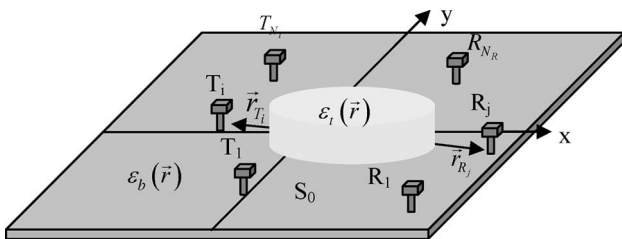
where $G(|\vec{r} - \vec{r}'|, f)$ is the Green function for a 2-D geometry $G(r) = (1/4j)H_0^{(2)}(kr)$, where $H_0^{(2)}(kr)$ is the second kind zero-order Hankel function and k is the wave number of the background reference medium. Under the Born approximation, we can substitute the equivalent current by the product of contrast and incident field. Using elementary transmitting antennas, the incident field can be described by Green functions centered in the transmitting elements positions

$$E_s\left(\vec{r}_{R_j}, f; \vec{r}_{T_i}\right) \cong -k^2 A_d \int_{V_0} c(\vec{r}; f) \cdot G(|\vec{r} - \vec{r}_{T_i}|, f)$$
$$\times G\left(|\vec{r}_{R_j} - \vec{r}|, f\right) dV \quad (3)$$

where A_d is a complex constant modelling the illumination field amplitude and phase, gain of antennas, and other system depending factors.

For the inverse imaging process based on UWB-BF, we may express the "frequency averaged contrast" $\tilde{c}$ as

$$\tilde{c}(\vec{r}) = A_i \sum_{f_{min}}^{f_{max}} \sum_{j=1}^{N_R} \sum_{i=1}^{N_T} \frac{E_s\left(\vec{r}_{R_j}, f; \vec{r}_{T_i}\right)}{k^2} \frac{1}{G(|\vec{r}_{T_i} - \vec{r}|, f)}$$
$$\times \frac{1}{G\left(|\vec{r}_{R_j} - \vec{r}|, f\right)}. \quad (4)$$

A_i is again a complex constant including multiple system factors and can be removed by appropriate calibration, using simple objects of well-known scattering characteristics.

The reconstruction algorithm forms every image point of the local electrical properties of the object by means of the synthesis of two focused groups (bifocusing) of antennas (transmitters and receivers). In (4), the received scattered fields resulting from all the antenna pairs are numerically weighted by a focusing operator so as to be focused on a unique object point. This numerical focusing operator [34] restores the amplitude and phase changes suffered by a wave in its way to and from every scattering point in the object. Applying this focusing operator to the measurement matrix for all the points of the image space grid, we are able to obtain a replica of the extended object. When highly inhomogeneous objects are observed, multiple and high-contrast scattering occurs. This results in nonlinear phenomena, which are frequency dependent, and consequently the continuous frequency superposition proposed in this paper will tend to smooth and reduce its effects, as will be shown in Section IV.

For 3-D geometries, the object inhomogeneities in the z-axis causes vertical (z-axis) diffraction and depolarization, and a vectorial formulation must be used based on the 3-D Green function $G(r) = e^{-jkr}/r$. In the case of

nonpenetrable objects, the contrast function can be easily related to the radar reflectivity image on the target surface, which is in fact an amplitude/phase expression of the object radar cross-section distribution. Both 2-D and 3-D radar images can be obtained in this way with very high spatial resolution if UWB signals are used [35], [36].

B. Sampling in Frequency- and Time-Domain UWB systems

Our aim is to obtain accurate spatial information of the electrically extended object, in terms of geometrical shape and electrical parameter values, using a network of antennas encircling the target.

Based on the Fourier diffraction theorem [37], the imaging problem can be stated as follows. The information obtained from the scattered field E_s produced by a particular frequency f_0 and orientation ϕ_0 [Fig. 2(a)] may be translated into a circle of radius $k = 2\pi f\sqrt{\mu_b \varepsilon_b}$ (semicircle TG for transmitting geometries and semicircle RG for reflection geometries) of the two-dimensional Fourier transform (FT) spectral domain (u, v) of the object $C(u, v) = FT\{c(x, y)\}$ [Fig. 2(b)]. The successive angular and frequency scans will fill the spectral domain "knowledge" on a specific manner depending on the imaging system design.

Under low-contrast electrical property conditions $|c(\vec{r})| \ll 1$, usually known as Born conditions, frequency and geometrical scans are partially equivalent and optimized combinations can be found to recover the contrast information of the object in spectral domain $C(u, v)$. In high contrast situations, those conditions are not applicable and new criteria need to be obtained.

1) Sampling in Frequency-Domain Systems: From the electromagnetic modal expansion of the fields scattered by an object when illuminated by an incident field, a minimum number of views N_ϕ is required to avoid loss of information. N_ϕ is equal to the number of coefficients of the cylindrical-mode (or spherical-mode for 3-D geometries) expansion of the scattered field. This results in a maximum angular step $\Delta\phi$, as shown in Table 1. Similarly, to avoid aliasing in the reconstructed image, a maximum
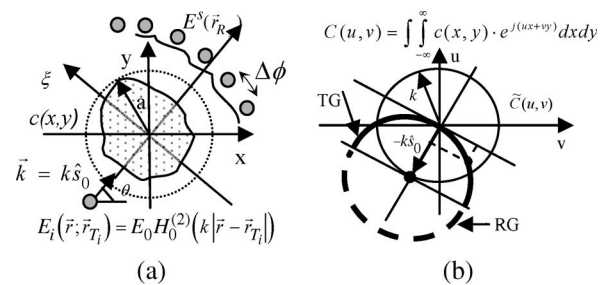

Fig. 2. *(a) Space and (b) spectral domain geometries.*

Table 1 Sampling Criteria for Frequency- and Time-Domain Systems With Respect to Minimum Wavelength $\lambda_{\min}$, Propagation Velocity c_0 in the Background Medium, Object Encircling Radius a, Margin for Delays Beyond the Target Dimensions δ_a, and Pulsed Systems Bandwidth B

Space sampling	FD sampling	TD sampling
$\Delta \phi \leq \lambda_{\min}/(2a)$	$\Delta f \leq \dfrac{c_0}{4(a+\delta_a)}$	$\Delta T \leq 1/2B$

frequency step must be chosen to accommodate the object relative delays, including possible object resonances able to extend the echo beyond the delay corresponding to target dimensions.

These sampling criteria hold for both nonpenetrable and penetrable objects. Notice that whereas the frequency step is only depending on the object size, the angular sampling must decrease when the frequency increases.

A conservative approach to design the UWB sensing array is to fulfill the minimum sampling criteria in the applicable acquisition domains for both the transmitting and the receiving elements in such a way that the complete scattering information is preserved and focusing ambiguities are avoided [38].

2) Sampling in Time-Domain Systems: In the case of time-domain UWB systems, very short pulses are typically used for illumination; the resulting scattered signals can be recorded by ultrafast interleaved analog-to-digital converters. Sampling speed is given by the usual Nyquist criterion depending on pulse bandwidth B, and the acquisition window must be chosen to accommodate the target echo duration, as is the case in frequency-domain systems.

In an ideal noiseless situation, time-domain (TD) and frequency-domain (FD) systems can be considered equivalent since results are Fourier transform pairs in usual low-power linear conditions. In practice, however, FD domain systems will benefit from the usually higher illumination energy/noise spectral density ratio of continuous-wave (CW) operation [39]. On the other hand, TD systems can overcome the possible isolation problems between transmitter and receiving antennas frequently affecting CW operation [40].

III. UWB RADAR IMAGING OF METALLIC OBJECTS

The approach described in Section II is first applied to perform radar imaging of nonpenetrable metallic objects. The idea is to review the imaging capabilities of a complex and electrically large metallic object using UWB interrogation signals [41]–[45].

1) Interrogation Geometry: Fig. 3 shows a metallized 1 : 48 scaled-down F-18 aircraft model and the amplitude of the horizontal-horizontal (HH) scattered field expressed in

radar cross-section (RCS) dBsm units. The scattered field is measured in the frequency domain according to the sampling criteria stated in Table 1 on a circular geometry around the object. In his FD system, the radial coordinate of Fig. 3(b) represents amplitude of the measured scattered field into the frequency range from 12 to 40 GHz (equivalent in relative terms to the 3.1–10.6 GHz band) that translates into an electrical object size in free space of 14 wavelengths at 12 GHz and 46.7 wavelengths at 40 GHz. Angle corresponds to the incidence angle with respect the F-18 fuselage axis in the horizontal plane, as shown in the figure. With respect to the general sensing geometry of Fig. 1, in this particular case $300(N_\phi \geq k_{f_{40\,\text{GHz}}}0.35 = 292)$ measurements arranged on a circumference surrounding the object and a monostatic case are considered.

Fig. 4 shows the echo returned by the F-18 model when illuminated frontally by an horizontally polarized 40 ps Gaussian pulse UWB signal. Notice that the echo extends beyond the target length due to the extinction of the
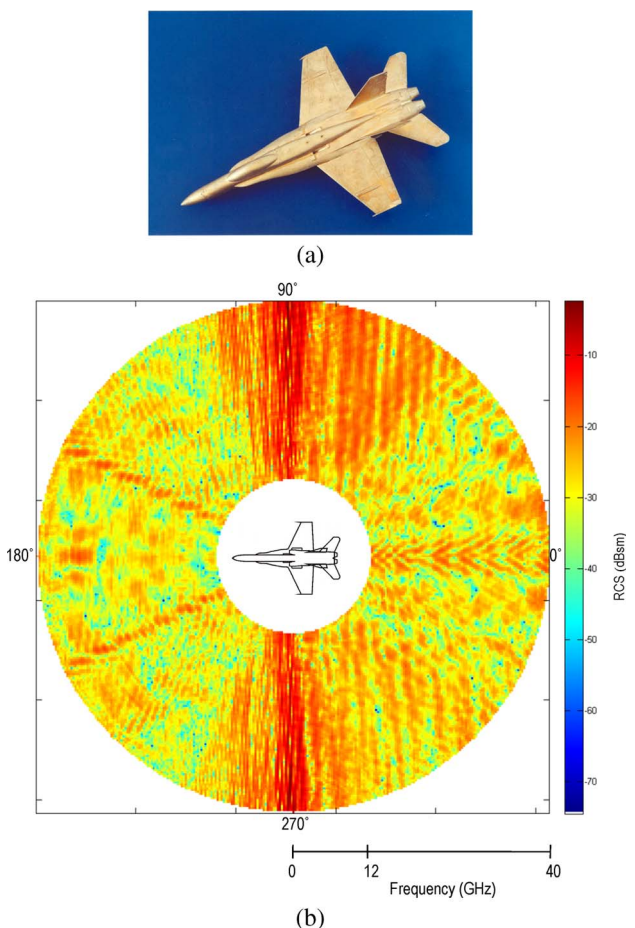

(a)

(b)

Fig. 3. *(a) Metallized 1 : 48 scaled-down F-18 model. (b) Amplitude of the scattered field normalized to its maximum RCS measured from 12 to 40 GHz expressed in polar coordinates (frequency, azimuth).*
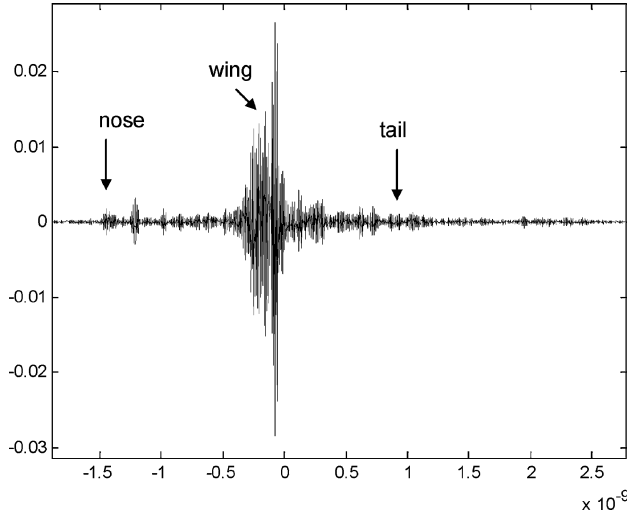
Fig. 4. *Time domain of the calculated echo returned by the F-18 model when illuminated frontally with a 40 ps Gaussian envelope pulse radiated by a UWB antenna with a bandwidth of 12–40 GHz. Horizontal time axis is labeled in nanoseconds. Vertical axis is the scattered electric field in V/m.*
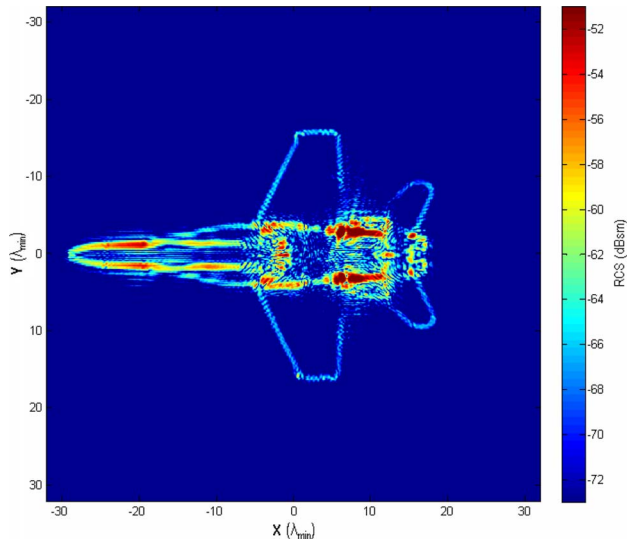

Fig. 5. *Image of F-18 obtained by processing the whole target spectral domain of Fig. 3. Only HH polarization is shown. Target dimensions are expressed normalized to the minimum measurement wavelength.*

internal resonances after illumination. The peak of the resulting echo corresponds to the wings, which at polarization HH interact strongly with the incident field.

2) Reflectivity Radar Imaging: From the scattered fields, radar images of the local reflectivity of the different target points can be obtained by use of the UWB-BF expression (4).
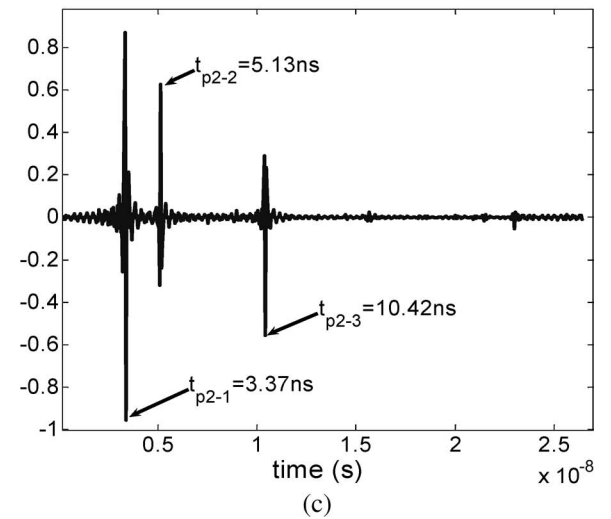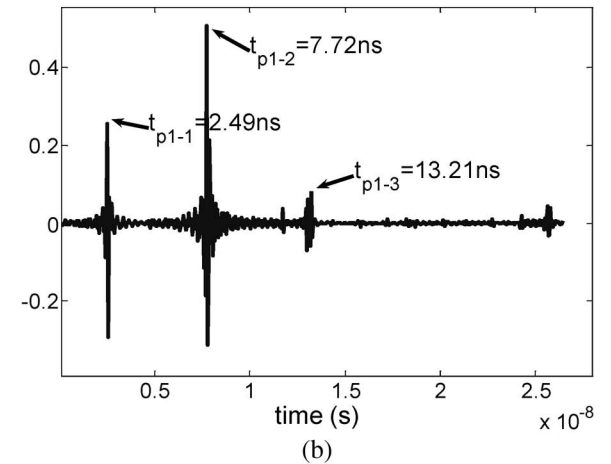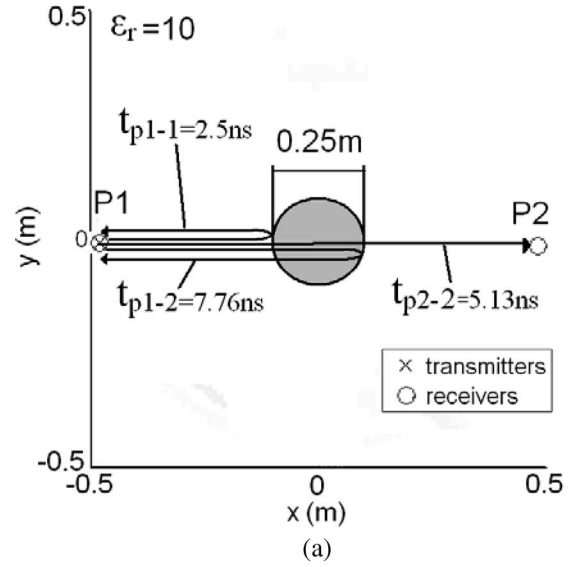

Fig. 6. *Time-domain response of dielectric cylinder (a) geometry, (b) received time-domain signal at P1 when P1 is transmitting, and (c) received time-domain signal at P2 when P1 is transmitting.*

Fig. 5 shows a high-resolution image of the F-18 model that clearly identifies the shape and main contributions of the object. The 2-D image corresponds to a vertical integration of the 3-D object. This image can be obtained in 3-D adding a third measurement dimension along the z-axis or elevation angle [36], although in most cases a 2-D image obtained from frequency-azimuth scattering integrating possible features in the z-dimension is sufficient for radar-target interaction analysis and much easier to represent.

In the very high-resolution conditions of UWB operation, all relevant scatterers are equally discriminated, and far- and near-field images are almost identical. This allows obtaining the target RCS by direct Fourier transform of the target image in the desired conditions of measurement [35].

3) Polarimetric Interferometric SAR Imaging: Although in the previous case we only presented the HH scattered field, actual measurements were fully polarimetric [46]. Applying appropriate angle and frequency windows to the UWB data set, the images can identify the main target scattering centers for the incidence angles and frequencies

of interest [47]. Similarly, a suitable polarimetric decomposition can be applied to the images for better understanding of the scattering mechanisms, for example, as a combination of canonical scatterers like sphere, dihedral, and helix [47]. With respect to conventional systems, UWB allows a much better spatial resolution for better scattering centers discrimination and analysis.

IV. TOMOGRAPHIC IMAGING

The general imaging approach described in Section II is now applied to perform tomographic imaging of penetrable objects. In this case, the potentiality of a UWB imaging system to see the internal characteristics of a penetrable object and its dependence on both size and contrast of the object will be discussed. As shown in (1), the object is seen through the induced currents that depend on both the contrast $c(\vec{r})$ function and the illuminating field $E(\vec{r}, f; \vec{r}_{T_i})$.

1) The Interrogation Parameters: In order to study the capability of a UWB signal to penetrate and properly visualize the internal structure of a contrasted extended
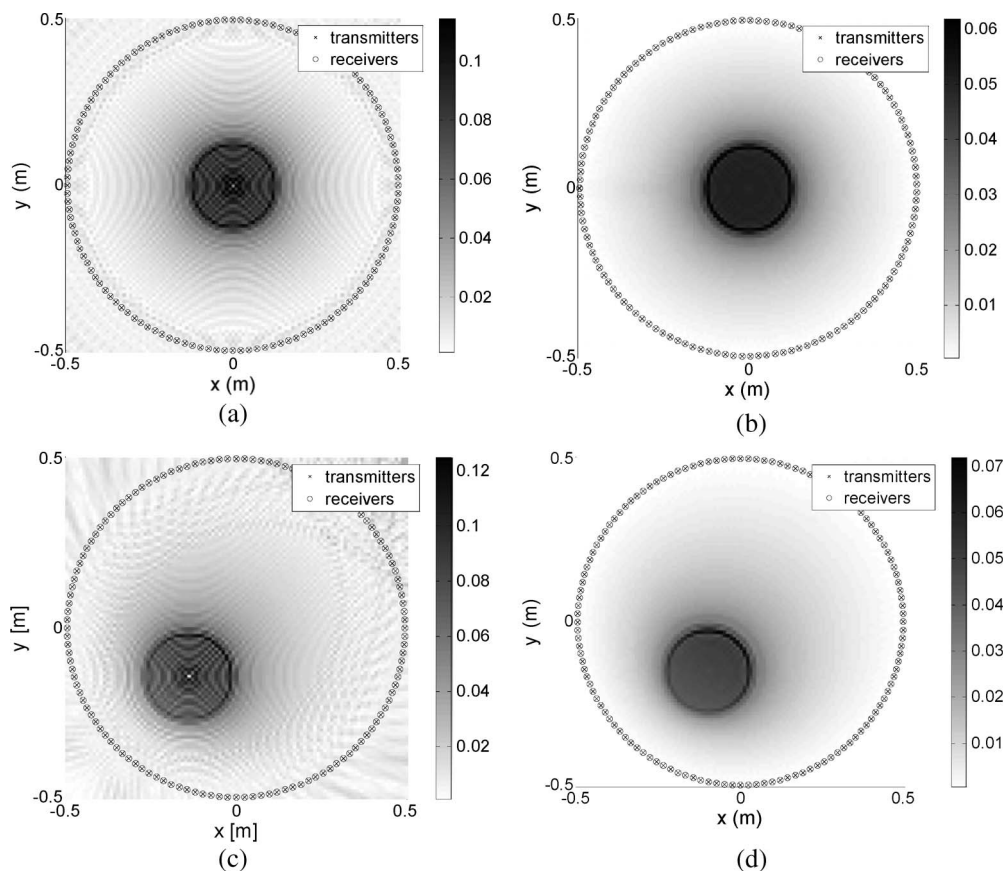

Fig. 7. *Reconstruction of a $\varepsilon_r = 100$ permittivity cylinder. (a) Center positioned at 10 GHz, (b) center positioned using the whole UWB 3.1–10.6 GHz, (c) off-center positioned at 10 GHz, and (d) off-center positioned using the whole UWB frequency range.*

object, a 2-D numerical test bed has been defined. The geometry consists on a circular 25-cm-diameter uniform object with different permittivity ranging from a very low contrasted object $(\varepsilon_r = 1.01)$ to a high contrasted one $(\varepsilon_r = 100)$. The frequency range has been chosen to be the 3.1–10.6 GHz band that translates into an electrical object size in free space of three wavelengths at 3.1 GHz and nine wavelengths at 10.6 GHz. The scattered field is measured with 128 sensors uniformly distributed over a 100-cm-diameter circular encircling geometry. Each sensor may act as transmitter or receiver. The total number of sensors has been chosen to verify angular sampling conditions according to Table 1 for the off-centered cylinder case $(N_\phi \geq 2k_{f_{10\,GHz}} 0.25 = 105)$.

This canonical object allows one to analytically compute the scattered fields. For a transmitter located at position $\vec{r}_{T_i}$, the scattered field at the receiver position $\vec{r}_{R_j}$ may be obtained from [48] after some particularization for the case of cylindrical illumination applied to dielectric objects

$$E_s\left(\vec{r}_{R_j}, f; \vec{r}_{T_i}\right) = \frac{k^2}{4\omega\varepsilon_b} \sum_{n=-\infty}^{\infty} H_n^{(2)}(kr_{T_i}) d_n H_n^{(2)}$$
$$\times \left(kr_{R_j}\right) e^{jn\left(\phi_{R_j} - \phi_{T_i}\right)}$$
$$d_n = \frac{-J_n(ka)}{H_n^{(2)}(ka)} \left[\frac{\frac{\varepsilon_t J_n'(k_t a)}{\varepsilon_b k_t a J_n(k_t a)} - \frac{J_n'(ka)}{ka J_n(ka)}}{\frac{\varepsilon_t J_n'(k_t a)}{\varepsilon_b k_t a J_n(k_t a)} - \frac{H_n^{(2)'}(ka)}{ka H_n^{(2)}(ka)}} \right]. \quad (5)$$

$B_n'(x) = B_{n-1} - (n/x)B_n$ $(B_n(x)$ are Bessel or Hankel functions, $J_n(x)$, $H_n^{(i)}(x))$; $k = \omega\sqrt{\mu_0\varepsilon_b}$, $k_t = \omega\sqrt{\mu_0\varepsilon_t}$.

Frequency and time responses related by Fourier transforms may give specific insights into the imaging process. As an example in Fig. 6(a), a general situation represented by test object and different positions of transmitters and receivers is depicted. The test object is the 25 cm cylinder with $\varepsilon_r = 10$, and two sensors are located at angular positions 180° and 0° and named as P1 and P2. Fig. 6(b) represents the time-domain evolution of scattered fields received at the P1 position for an incident 3.1–10.6 GHz bandwidth pulse transmitted from P1. Fig. 6(c) shows the evolution of the time-domain signal received at P2 when sensor P1 is transmitting. Major contributions may be identified and their arrival time and relative amplitude specified. In Fig. 6(b), the two first reflection contributions t_{P1-1} and t_{P1-2} corresponding to the reflections in the first and second boundaries as seen from the P1 sensor position may be identified. In Fig. 6(c), the two first transmission contributions t_{P2-1} and t_{P2-2} corresponding to the propagation through the cylinder external and internal paths, seen at P2 sensor position, may also be identified. For this particular contrast case, reflection and transmission values are in

the same order of magnitude. Lower permittivity values produce higher transmission values and higher permittivity result on higher reflection scattered field values. From the simulated scattered fields given by (5), the use of (4)
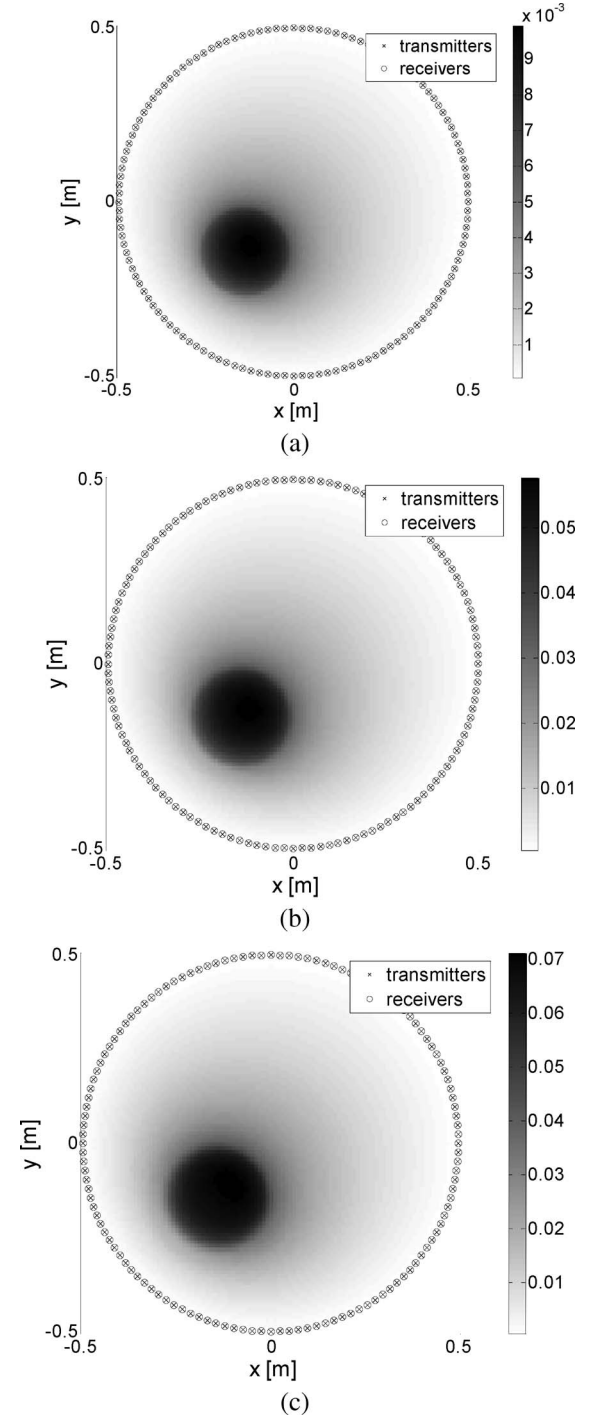

Fig. 8. *UWB reconstruction of an off-center frequency dispersive cylinder of radius 0.125 m. (a) $\varepsilon_t = 1.01$, (b) $\varepsilon_t(f) = 1.31 - 0.03f_{GHz}$, and (c) $\varepsilon_t(f) = 1.51 - 0.05f_{GHz}$.*
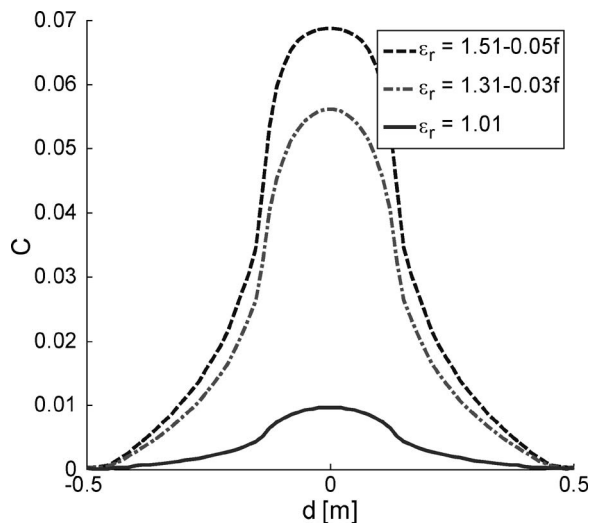
Fig. 9. *UWB cylinder transversal cross-section reconstruction comparison for the previous frequency dispersive profiles.*

allows one to reconstruct the object contrast given by $c = J_{eq}/j\omega\varepsilon_b E$.

2) Narrow-Band Versus Wide-Band Performance: Under low-contrast Born objects, frequency and spatial scanning are partially equivalent (giving almost equivalent information), and optimized combinations of space and frequency sampling can be found to fill the object spectral domain and thus to obtain its correct image. In this low-contrast case, a single frequency and a dense angular sampling may be equivalent to a dense frequency sampling combined with a reduced number of views. Under non-Born conditions, UWB proves to succeed in obtaining high-quality images, whereas it is not possible using a single frequency.

Fig. 7 shows how for high-contrast objects the UWB frequency scan [Fig. 7(b)] improves the quality of the monofrequency reconstruction [Fig. 7(a)] for a center positioned cylinder. Fig. 7(c) and (d) shows how the same improvement in quality of the UWB reconstruction can be maintained for an off-centered cylinder. The off-centered cylinder is a more challenging geometry as the inherent symmetry of the system is broken. Notice also that the monofrequency reconstruction is clearly affected by a Moiré pattern that disappears in the UWB frequency image.

3) Dielectric Frequency Dispersion: One of the concerns in performing wide-band imaging is the influence of the permittivity variations with frequency. In order to assess this effect in imaging, three different linear frequency profiles have been analyzed: (a) $\varepsilon_t = 1.01$, (b) $\varepsilon_t(f) = 1.31 - 0.03 f_{\text{GHz}}$, and (c) $\varepsilon_t(f) = 1.51 - 0.05 f_{\text{GHz}}$ corresponding to variations of 0%, 30%, and 40%,

respectively, relative to the initial 3 GHz permittivity values These relative variations correspond to the range of variations found in human breast biological tissues [49].

Fig. 8 shows the reconstructed image corresponding to the different frequency profiles previously defined for the case of an off-center 25 cm diameter cylinder. As may be seen, the object location, size, and profile are properly reconstructed. Internal inspection (Fig. 9) shows that the reconstructed section for the three profiles is not affected by the dispersion, with quantitative values corresponding approximately to the frequency averaged values.

4) Monostatic Versus Multistatic Geometry Performance: In the previous section, we have presented the potentiality of an UWB radar system to perform a tomographic image of a high-contrast object. The objective here is to analyze how different sensing approaches affect the
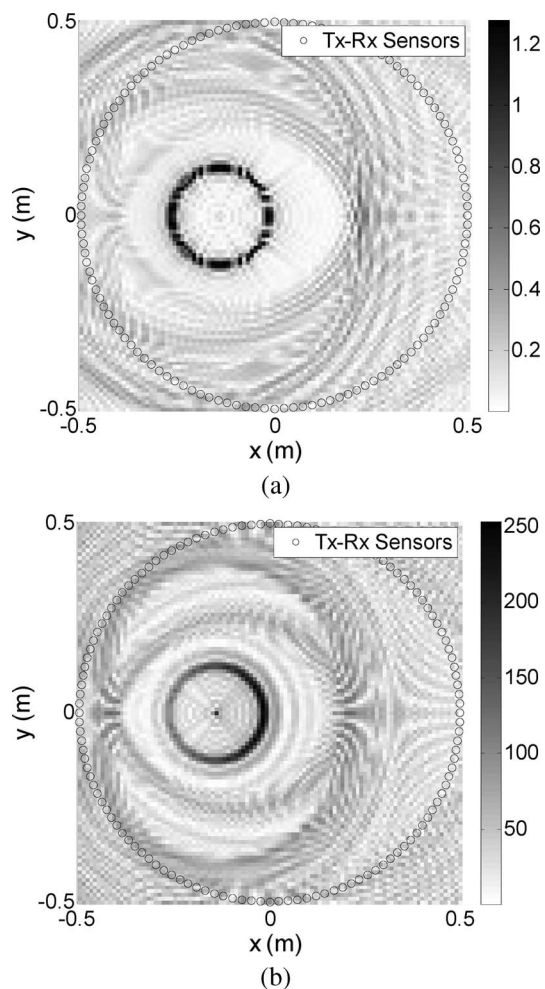

Fig. 10. *Multiple monostatic permittivity reconstruction for a cylinder of 25 cm diameter and dielectric permittivity of (a) $\varepsilon_t = 1.01$ (upper) and (b) $\varepsilon_t = 100$ (lower).*

quality of the image. Two test cases are considered: a low-contrast $(\varepsilon_t = 1.01)$ and a high-contrast $(\varepsilon_t = 100)$ 25-cm-diameter cylinder. The test geometry is the previously described consisting on 128 sensors. The center of the object cylinder is displaced 10 cm of the center of the measurement geometry.

Fig. 10 shows the UWB reconstruction obtained in the monostatic case for both cylinders using the 128 sensors. That is, each sensor only receives the backscattered field produced by its own illuminating field. The results for both cases show that only the perimeter of the object is reconstructed, and also it is not possible to actually reconstruct the values of the permittivity inside the object. According to the diffraction theorem in Section II, in the case of the monostatic geometry, only the high frequencies of the object spectral domain located on the external semicircle (RG line in Fig. 2) are effectively recovered, while the low frequencies of the object spectral domain are lost. Accordingly, the reconstructed image, regardless of the contrast values, is in all cases a high-pass version of the real object, which was also the case in the aircraft monostatic radar image of Fig. 5. The result is only abrupt changes in the object, as in this case where the borders are reconstructed, while the fairly constant internal structure is completely missed.

5) Multistatic Extend of the Interrogation Geometry: To improve the imaging capability of the sensing geometry, it is then necessary to evolve from the monostatic to the multistatic geometry. In the multistatic geometry, one sensor acts as a transmitter and the scattered field is measured by all the available sensors. A full scanning is achieved when all sensors have acted as transmitters. In order to analyze the effect of the multistatic angular extent of the interrogation geometry, a circular high contrasted $(\varepsilon_t = 100)$ extended object (25 cm diameter) has been investigated for different encircling angular sectors ranging from $\pm 3°$ up to the whole encircling geometry of $\pm 180°$.

It can be seen in Fig. 11 how the reconstructed image progresses from just the border reconstruction corresponding to the initial quasi-monostatic case until reaching a well-behaved internal structure reconstruction for the whole encircling geometry.

Fig. 12 shows the reconstructed section for the different cases. It is clearly seen that a scanning geometry of $\pm 135°$ already offers very good reconstruction.

It is also of interest to consider the case of the off-centered cylinder. Fig. 13 shows the last two scanning cases represented in Fig. 11 for an off-centered cylinder. When compared to the monostatic cases of Fig. 5, the
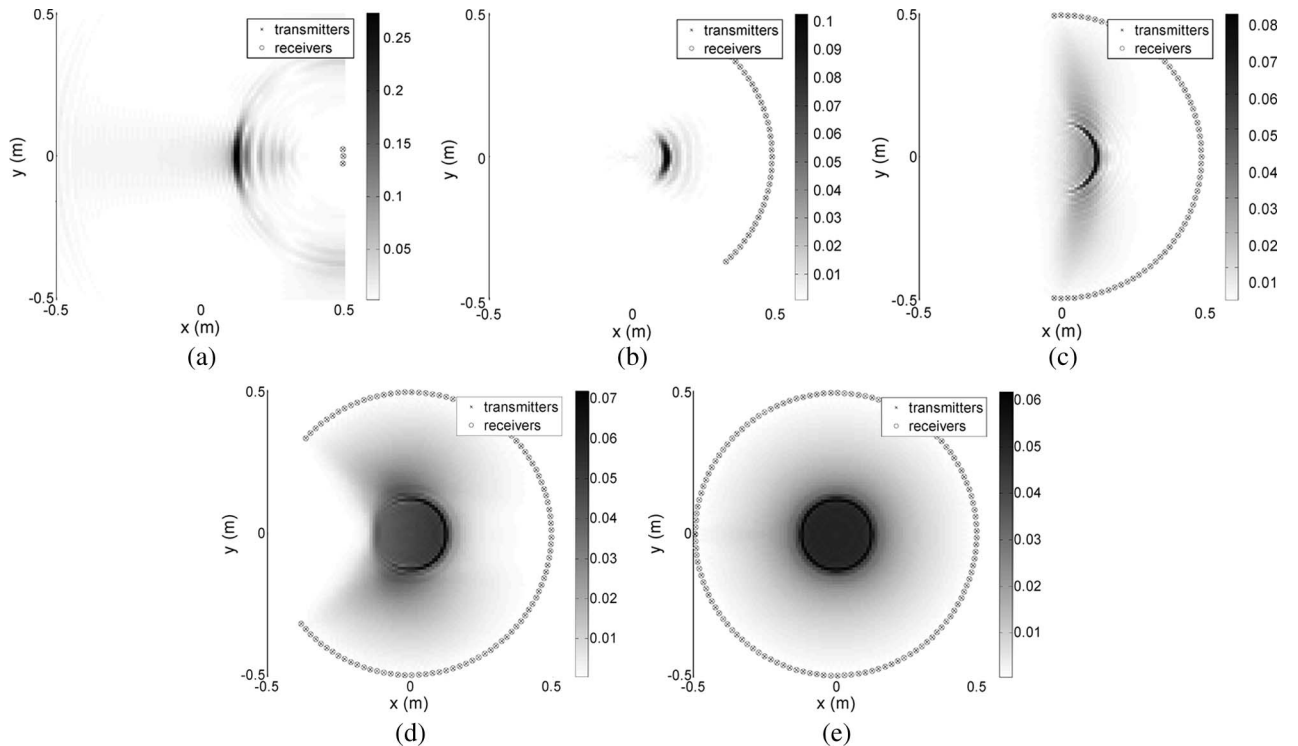

Fig. 11. *Reconstruction of a cylinder of radius 0.125 m and $\varepsilon_t = 100$ using the UWB-BF method for (a) $\pm 3°$ encircling sensor geometry, (b) a $\pm 45°$ encircling sensor geometry, (c) $\pm 90°$ encircling sensor geometry, (d) $\pm 135°$ encircling sensor geometry, and (e) a completely encircling sensor geometry.*
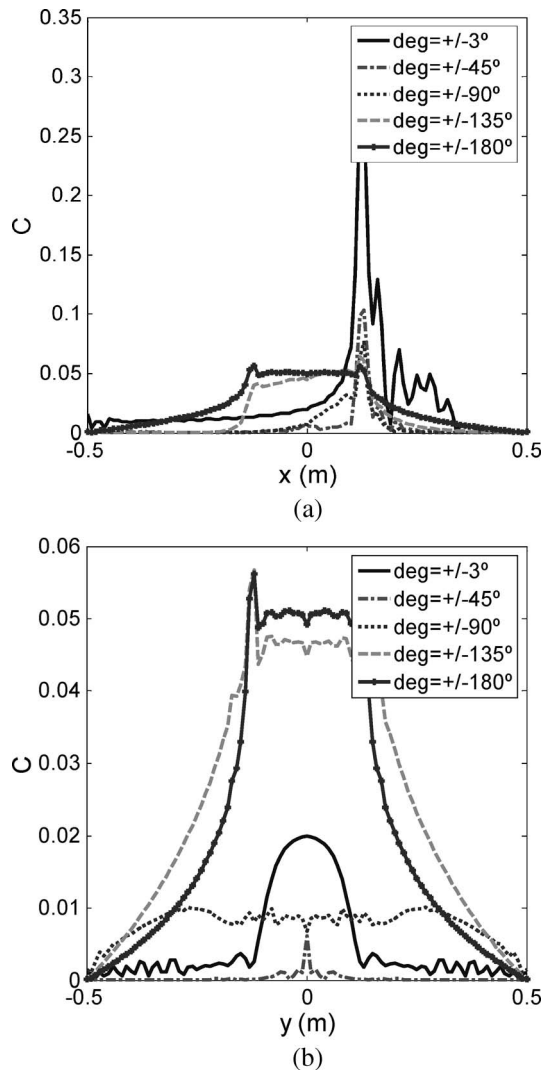
(a)

(b)

Fig. 12. *Cylinder reconstruction comparison for the sensing geometries of Fig. 11: (a) y = 0 and (b) x = 0.*

superior quality of the image is evident even for the challenging case of high-contrast objects.

6) Multistatic Transmission Versus Reflection Geometry: Once the multistatic architecture has been proven as more appropriate for imaging purposes, and the effect of the angular dimension of the encircling sensor studied, it seems convenient to investigate the effect of transmission versus reflection geometry on the quality of reconstruction. The interrogation architecture for this case consists of a set of transmitters and receivers placed opposite on a circumference that surrounds the object under investigation. Only transmission is considered, that is, back-scattered fields are not measured. In this case, this object is the high contrasted ($\varepsilon_r = 100$) 25-cm-diameter cylinder. The transmitting and receiving angular sectors are progressively increased from $\pm 3°$ [Fig. 14(a)], up to the

$\pm 135°$ [Fig. 14(d)]. The result for the whole encircling geometry of $\pm 180°$ has been shown in Fig. 7(b). The results are shown with an indication of the transmitted and receiver sensors.

The reconstructed images for the different cases show that the external structure is properly reconstructed with the $\pm 90°$ sensing geometry and that for most of the cases a geometry between $\pm 90°$ and $\pm 135°$ could be the optimum choice in the sense that a good image is produced with a reduced number of sensors, even for a high-contrast object.

Fig. 15 shows the reconstructed section for the different sensing geometries of Fig. 14. Comparing the results with those of Fig. 12, it is clear that transmission-only measurements offer an equivalent quality of the reconstruction to that of multistatic reflection measurements.
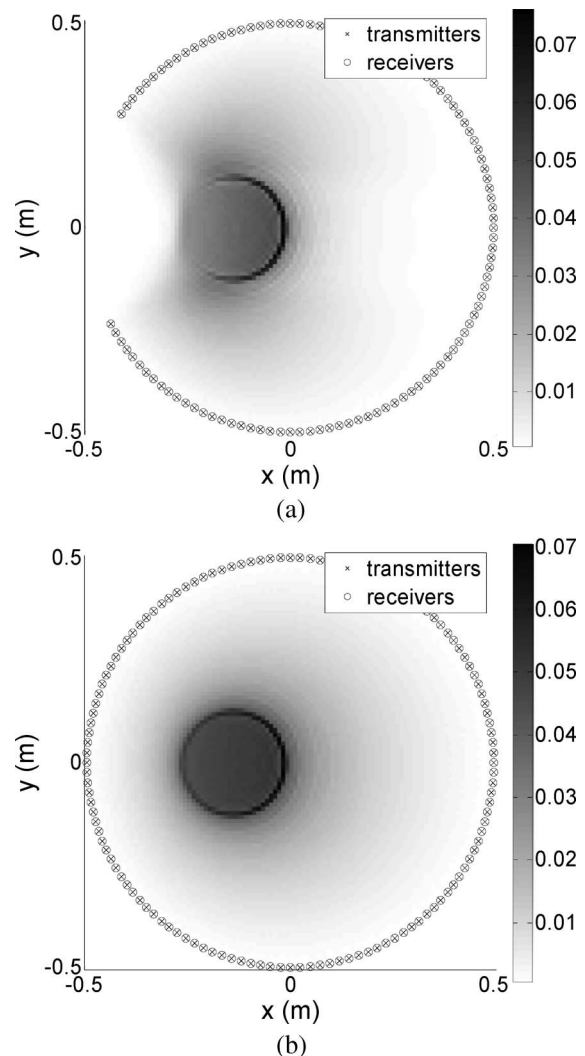

(a)

(b)

Fig. 13. *Reconstruction of an off-centered cylinder of radius 0.125 m and $\varepsilon_t = 100$ using the UWB-BF method for (a) $\pm 135°$ and (b) a completely encircling sensor geometry.*
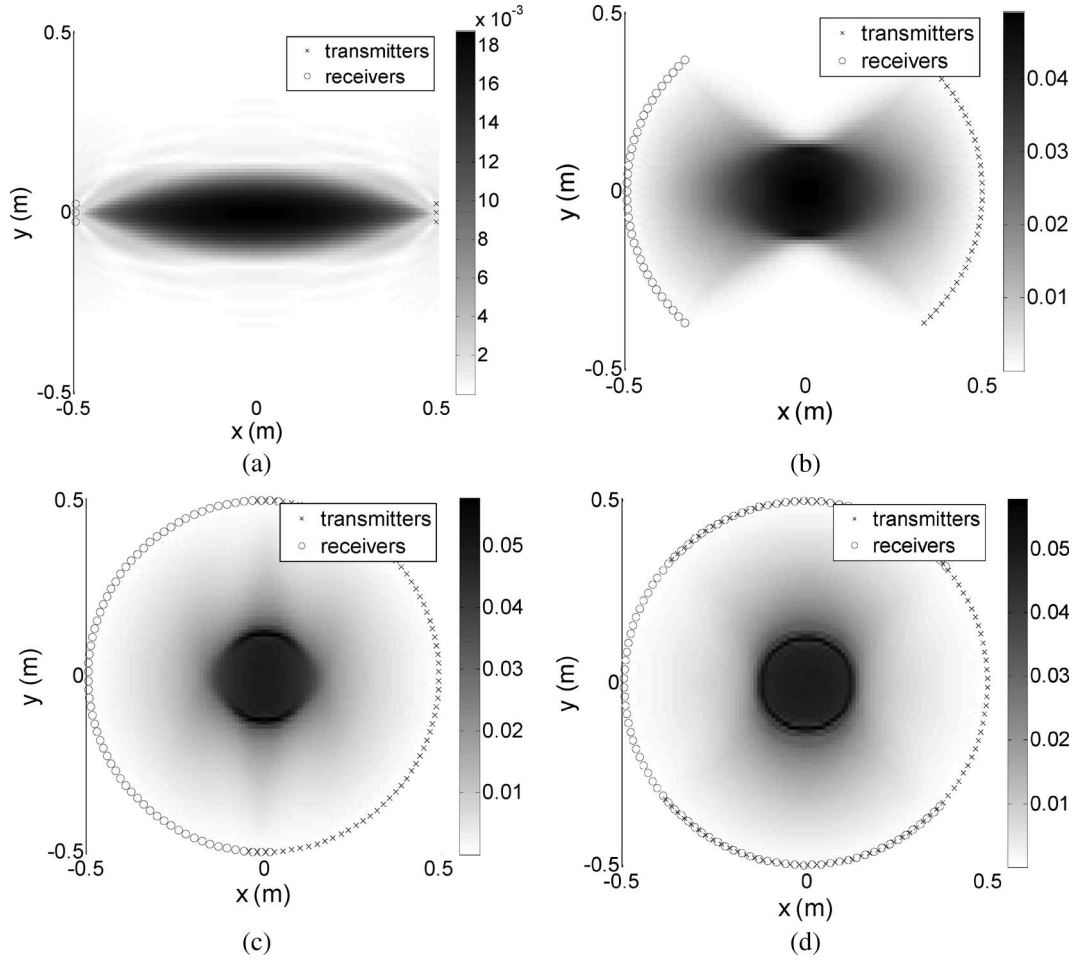
(a)

(b)

(c)

(d)

Fig. 14. *Reconstruction of a cylinder of radius 0.125 m and $\varepsilon_t = 100$ using the UWB-BF method for (a) a $\pm 3°$ transmission sensor geometry, (b) $\pm 45°$ transmission sensor geometry, (c) a $\pm 90°$ transmission sensor geometry, and (d) a $\pm 135°$ transmission sensor geometry.*
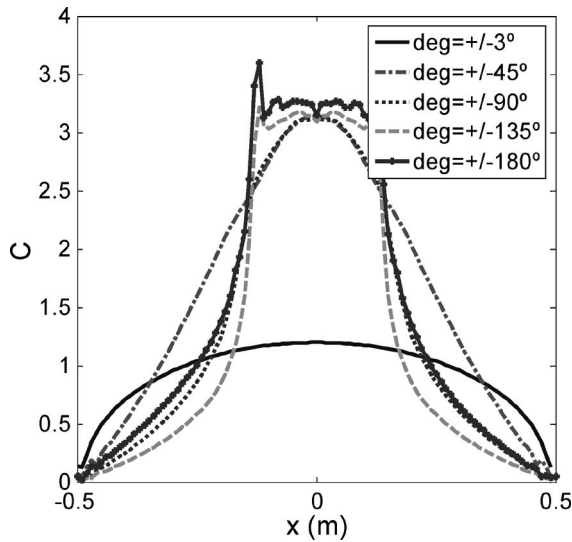
7) Experimental Results: In order to perform an experimental validation of the previous imaging results, UWB measurements (3.1–10.6 GHz) have been done. Measurements were taken inside an anechoic chamber in order to avoid an excessive reflection from the environment. The sensing geometry (Fig. 16) consisted of two parallel linear arrays spaced 1.4 m. The arrays are synthesized by placing an antenna on a linear robotic
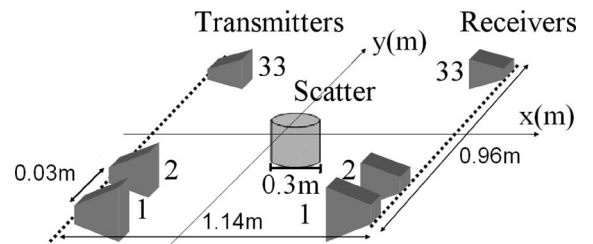

Fig. 15. *Cylinder reconstruction comparison at $y = 0$ for the previous transmission sensor geometries of Fig. 14.*

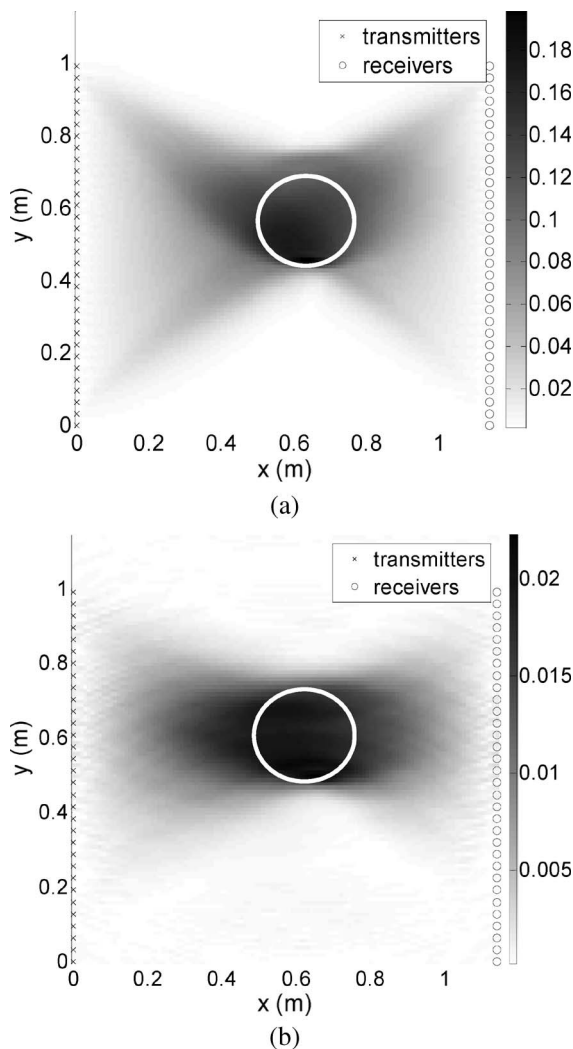**Fig. 16.** *Geometry of the experimental setup.*

Fig. 17. *Reconstruction of a water cylinder 0.15 m radius using the UWB-BF imaging method for the geometry of Fig. 16.*
(a) Theoretical reconstruction and (b) experimental reconstruction.

arm and moving it to different locations. The antennas that were used for the measurement were UWB ridge horn antennas. Each synthetic array had 33 points spaced 0.03 m. The test object was a 0.3-m-diameter cylinder 10 cm *x*-axis off center filled with water.

The scanning geometry is equivalent to the limited transmission geometry of Fig. 14(b) with the difference that the sensors are placed on a linear segment instead of a circular arc.

Comparison of the theoretical results [Fig. 17(a)] obtained by simulation and the experimental results [Fig. 17(b)] clearly demonstrates the validity of the simulation method for imaging purposes. It is also clear that within the limitations set by reduced dimension of the scanning geometry, it is possible to correctly locate the position of the cylinder, and a uniform reconstruction is achieved.

V. CONCLUSION

UWB electromagnetic sensing provides a set of unique possibilities in terms of resolution and robustness for radar tomographic imaging. The UWB bifocusing operator provides a general framework to employ arbitrary sensing geometries.

UWB short-range imaging is possible for both impenetrable (metallic) objects as well as for low- and high-contrast penetrable objects under a certain sampling criteria for frequency and spatial scanning. For nonpenetrable targets, monostatic encircling geometries provide very high-quality reflectivity images.

In tomographic applications of penetrable objects, numerical simulations and measurements show that good results are obtained with multistatic transmission sensing geometries that do not require to completely enclosing the sensing region. UWB-BF has also been shown to be robust in front of frequency dispersion of the permittivity values.

For low-contrast objects, optimization on the established criteria can be applied, as frequency and geometrical data are partially equivalent under the Born approximation. For high-contrast objects, simultaneous accomplishment of the two sampling criteria (frequency and angle) gives better reconstructed images due to the nonresonant characteristic of the UWB illuminating field.

In both cases, impenetrable and penetrable objects, resolution can reach $\lambda/2$, at the highest operating frequency, in all directions for geometries enclosing the object to be imaged. ∎

REFERENCES

[1] R. K. Mueller, M. Kaveh, and G. Wade, "Reconstructive tomography and applications to ultrasonics," *Proc. IEEE*, vol. 67, pp. 567–587, Apr. 1979.

[2] A. J. Devaney, "A computer simulation study of diffraction tomography," *IEEE Trans. Biomed. Eng.*, vol. BE-30, pp. 377–386, Jul. 1983.

[3] A. J. Devaney, "Geophysical diffraction tomography," *IEEE Trans. Geosci. Remote Sens.*, vol. GRS-22, pp. 3–13, Jan. 1984.

[4] S. X. Pan and A. C. Kak, "A computational study of reconstruction algorithms for diffraction tomography: Interpolation versus filtered backpropagation," *IEEE Trans. Acoust., Speech, Signal Process.*, vol. ASSP-31, pp. 1262–1275, Oct. 1983.

[5] R. Zoughi, *Microwave Testing and Evaluation*. Amsterdam, The Netherlands: Kluwer, 2000.

[6] J. C. Bolomey, *Frontiers in Industrial Process Tomography*. London, U.K.: Engineering Foundation, 1995.

[7] L. E. Larsen and J. H. Jacobi, Eds., *Medical Applications of Microwave Imaging*. Piscataway, NJ: IEEE Press, 1986.

[8] E. C. Fear, P. M. Meaney, and M. A. Stuchly, "Microwaves for breast cancer detection," *IEEE Potentials*, vol. 22, p. 12, Feb./Mar. 2003.

[9] M. Pastorino, "Short-range microwave inverse scattering techniques for image reconstruction and applications," *IEEE Trans. Instrum. Meas.*, vol. 47, p. 1419, Dec. 1998.

[10] J. D. Taylor, Ed., *Introduction to Ultra-Wideband Radar Systems*. Boca Raton, FL: CRC Press, 1995.

[11] R. Zetik, J. Sachs, and R. S. Thomä, "UWB short-range radar sensing," *IEEE Instrum. Meas. Mag.*, pp. 39–45, Apr. 2007.

[12] F. C. Chen and W. C. Chew, "Time-domain ultra-wideband microwave imaging radar system," in *Proc. 15th IEEE Instrum. Meas. Technol. Conf., 1998 (IMTC/98)*, May 18–21, 1998, vol. 1, pp. 648–650.

[13] A. E. C. Tan and M. Y. W. Chia, "Measuring human body impulse response using UWB radar," *Electron. Lett.*, vol. 41, no. 21, pp. 1193–1194, Oct. 2005.

[14] S. Gezici, Z. Tian, G. B. Giannakis, H. Kovayashi, A. F. Molisch, H. V. Poor, and Z. Sahinoglu, "Localization via ultra-wideband radios," *IEEE Signal Process. Mag.*, vol. 22, pp. 70–84, Jul. 2005.

[15] C. Sturm, W. Sorgel, T. Kayser, and W. Wiesbeck, "Deterministic UWB wave propagation modeling for localization applications based on 3D ray tracing," in *Proc. IEEE MTT-S Int. Microwave Symp. Dig.*, 2006, pp. 2003–2006.

[16] J. J. Lee and S. Singh, "Using UWB radios as sensors for disaster recovery," in *Proc. IEEE Conf. Ultra-Wideband*, 2007, pp. 311–315.

[17] R. F. Xue, B. Yuan, and J. F. Mao, "Application of diffraction technology to UWB SAR research," in *Proc. IEEE Radar Conf.*, pp. 492–497.

[18] S. Hantscher, A. Reisenzahn, and C. G. Diskus, "Through-wall imaging with a 3-D UWB SAR algorithm," *IEEE Signal Process. Lett.*, vol. 15, pp. 269–272, 2008.

[19] J. Modelski, M. Bury, and Y. Yashchyshyn, "Short-pulse microwave imaging system," in *Proc. 5th Int. Conf. Microw. Electron.: Meas., Identif., Applicat. 2005 (MEMIA '05)*, Dec. 13–15, 2005, pp. 31–36.

[20] E. C. Fear, X. Li, S. C. Hagness, and M. A. Stuchly, "Confocal microwave imaging for breast cancer detection: Localization of tumors in three dimensions," *IEE Trans. Biomed. Eng.*, vol. 49, pp. 812–822, Aug. 2002.

[21] E. J. Bond, L. Xu, S. C. Hagness, and B. D. Van Veen, "Microwave imaging via space-time beamforming for early detection of breast cancer," *IEEE Trans. Antennas Propag.*, vol. 51, pp. 1690–1705, Aug. 2003.

[22] A. Broquetas, J. Romeu, J. M. Rius, A. Elias, A. Cardama, and L. Jofre, "Cylindrical geometry: A further step in active microwave tomography," *IEEE Trans. Microwave Theory Tech.*, vol. 19, pp. 836–844, May 1991.

[23] J. M. Rius, C. Pichot, L. Jofre, J. C. Bolomey, N. Joachimowicz, A. Broquetas, and M. Ferrando, "Planar and cylindrical active microwave temperature imaging: Numerical simulations," *IEEE Trans. Med. Imag.*, vol. 11, pp. 457–469, Dec. 1992.

[24] A. Joisel, J. Mallorqui, A. Broquetas, J. M. Geffrin, N. Joachimowicz, M. Vall-llossera, L. Jofre, and J. C. Bolomey, "Microwave imaging techniques for biomedical applications," in *Proc. 16th IEEE Instrum. Meas. Technol. Conf. 1999 (IMTC/99)*, May 24–26, 1999, vol. 3, pp. 1591–1596.

[25] T. C. Guo and W. W. Guo, "High resolution microwave imaging simulation of human neck," in *Proc. 16th IEEE Instrum. Meas. Technol. Conf. 1999 (IMTC/99)*, May 24–26, 1999, vol. 3, pp. 1586–1590.

[26] S. Y. Semenov, A. E. Bulyshev, A. Abubakar, V. G. Posukh, Y. E. Sizov, A. E. Souvorov, P. M. van den Berg, and T. C. Williams, "Microwave-tomographic imaging of the high dielectric-contrast objects using different image-reconstruction approaches," *IEEE Trans. Microwave Theory Tech.*, vol. 53, pp. 2284–2294, Jul. 2005.

[27] A. Fhager, P. Hashemzadeh, and M. Persson, "Reconstruction quality and spectral content of an electromagnetic time-domain inversion algorithm," *IEEE Trans. Biomed. Eng.*, vol. 53, pp. 1594–1604, Aug. 2006.

[28] N. N. Qaddoumi, M. Abou-Khousa, and W. M. Saleh, "Near-field microwave imaging utilizing tapered rectangular waveguides," *IEEE Trans. Instrum. Meas.*, vol. 55, pp. 1752–1756, Oct. 2006.

[29] A. G. Yarovoy, T. G. Savelyev, P. J. Aubry, P. E. Lys, and L. P. Lighart, "UWB array-based sensor for near-field imaging," *IEEE Trans. Microwave Theory Tech.*, vol. 55, pp. 1288–1295, Jun. 2007.

[30] A. Papió, J. M. Jornet, P. Ceballos, J. Romeu, S. Blanch, A. Cardama, and L. Jofre, "UWB short range imaging," in *Proc. III Int. Conf. Electromagn. Near-Field Characterization Imag.*, St. Louis, MO, 2007.

[31] M. Benedetti, M. Donelli, A. Martini, M. Pastorino, A. Rosani, and A. Massa, "An innovative microwave-imaging technique for nondestructive evaluation: Applications to civil structures monitoring and biological bodies inspection," *IEEE Trans. Instrum. Meas.*, vol. 55, pp. 1878–1884, Dec. 2006.

[32] G. A. Tsihrintzis and A. J. Devaney, "Higher-order (nonlinear) diffraction tomography: Reconstruction algorithms and computer simulation," *IEEE Trans. Image Process.*, vol. 9, pp. 1560–1572, Sep. 2000.

[33] R. F. Harrington, *Time-Harmonic Electromagnetic Fields*. New York: McGraw-Hill, 1961.

[34] Y. J. Kim, L. Jofre, F. De Flaviis, and M. Q. Feng, "Microwave reflection tomographic array for damage detection of civil structures," *IEEE Trans. Antennas Propag.*, vol. 51, pp. 3022–3032, Nov. 2003.

[35] A. Broquetas, J. Palau, L. Jofre, and A. Cardama, "Spherical wave near-field imaging and radar cross section measurement," *IEEE Trans. Antennas Propag.*, vol. 46, pp. 730–735, May 1998.

[36] X. Anguela and A. Broquetas, "A near-field 3D radar imaging technique," in *Proc. 23rd Eur. Microw. Conf.*, Madrid, Spain, Sep. 1993, pp. 377–379.

[37] M. Slaney and A. C. Kak, "Limitations of imaging with first-order diffraction tomography," *IEEE Trans. Microwave Theory Tech.*, vol. MTT-32, Aug. 1984.

[38] L. Jofre, A. Papio, J. M. Jornet, P. Ceballos, J. Romeu, S. Blanch, and A. Cardama, "UWB short range bi-fousing tomographic imaging," *IEEE Trans. Instrum. Meas.*, 2008.

[39] A. G. Yarovoy and L. P. Ligthart, "Ultra-wideband technology today," in *Proc. 15th Int. Conf. Microw., Radar Wireless Commun., 2004 (MIKON-2004)*, May 17–19, 2004, vol. 2, pp. 456–460.

[40] F. T. Talom, B. Uguen, L. Rudant, J. Keignart, J. F. Pintos, and P. Chambelin, "Evaluation and characterization of an UWB antenna in time and frequency domains," in *Proc. 2006 IEEE 2006 Int. Conf. Ultra-Wide Band*, Sep. 2006, pp. 669–673.

[41] S. Kidera, T. Sakamoto, and T. Sato, "A high-resolution 3-D imaging algorithm with linear array antennas for UWB pulse radar systems," in *Proc. IEEE Antennas Propag. Soc. Int. Symp. 2006*, Jul. 9–14, 2006, pp. 1057–1060.

[42] A. Farina, F. A. Studer, and R. Vitiello, "High resolution radar for enhanced target detection," in *Proc. Radar 92 Int. Conf.*, Oct. 12–13, 1992, pp. 163–166.

[43] S. P. Jacobs and J. A. O'Sullivan, "Automatic target recognition using sequences of high resolution radar range-profiles," *IEEE Trans. Aerosp. Electron. Syst.*, vol. 36, no. 2, pp. 364–381, Apr. 2000.

[44] V. Kovalenko, A. Yarovoy, and L. P. Ligthart, "Waveform based detection of anti-personnel mines with an UWB radar," in *Proc. IEEE Int. Conf. Ultra-Wideband 2005 (ICU 2005)*, Sep. 5–8, 2005, pp. 644–649.

[45] N. C. Currie, *Radar Reflectivity Measurement*. Norwood, MA: Artech House, 1989.

[46] X. Fabregas, J. Romeu, A. Broquetas, and L. Jofre, "Target spinor calibration for polarimetric radar cross section measurements," *Electron. Lett.*, vol. 31, pp. 1694–1695, Sep. 1995.

[47] X. Fabregas, A. Broquetas, J. Romeu, and L. Jofre, "Study of complex targets using polarimetric ISAR techniques," in *Proc. 2nd Int. Workshop Radar Polarimetry*, Nantes, France, 1992, pp. 535–546.

[48] C. A. Balanis, *Advanced Engineering Electromagnetics*. New York: Wiley, 1989.

[49] M. Lazebrik, L. McCartney, D. Popovic, C. B. Watkins, M. J. Lindstrom, J. Harter, S. Sewall, A. Magliocco, J. H. Booske, M. Okoniewski, and S. C. Hagness, "A large-scale study of the ultrawideband microwave dielectric properties of normal breast tissue obtained from reduction surgeries," *Phys. Med. Biol.*, vol. 52, pp. 2637–2656, 2007.

ABOUT THE AUTHORS

Lluís Jofre (Senior Member, IEEE) was born in Mataró, Spain, in 1956. He received the M.Sc. (Ing.) and Ph.D. (Dr.Ing.) degrees in electrical engineering (telecommunications engineering) from the Universitat Politècnica de Catalunya (UPC), Barcelona, Spain, in 1978 and 1982, respectively.

From 1979 to 1980, he was Research Assistant with the Electrophysics Group, UPC, where he worked on the analysis and near-field measurement of antenna and scatterers. From 1981 to 1982, he joined the Ecole Superieure d'Electricite, Paris, France, where he was involved in microwave antenna design and imaging techniques for medical and industrial applications. In 1982, he became an Associate Professor in the Communications Department, Telecommunication Engineering School, UPC, where he became a full Professor in 1989. From 1986 to 1987, he was a Visiting Fulbright Scholar at the Georgia Institute of Technology, Atlanta, working on antennas and electromagnetic imaging and visualization. From 1989 to 1994, he was Director of the Telecommunication Engineering School, UPC; and from 1994–2000, UPC Vice-rector for Academic Planning. From 2000 to 2001, he was a Visiting Professor with the Electrical and Computer Engineering Department, Henry Samueli School of Engineering, University of California. From 2002 to 2004, he was Director of the Catalan Research Foundation; since 2003, he has been Director of the UPC-Telefonica Chair. His research interests include antennas, electromagnetic scattering and imaging, and system miniaturization for wireless and sensing industrial and bio applications. He has published more than 100 scientific and technical papers, reports, and chapters in specialized volumes.

Antoni Broquetas (Member, IEEE) was born in Barcelona, Spain, in 1959. He received the Ing. degree in telecommunication engineering and the Dr.Ing. degree in telecommunications engineering from the Universitat Politècnica de Catalunya (UPC), Barcelona, in 1985 and 1989, respectively.

In 1986, he was a Research Assistant with Portsmouth Polytechnic, Portsmouth, U.K., involved in propagation studies. In 1987, he joined the Department of Signal Theory and Communications, School of Telecommunication Engineering, UPC. From 1998 to 2002, he was Subdirector of Research with the Institute of Geomatics, Barcelona. Since 1999, he has been a full Professor at UPC, involved in research on radar imaging and remote sensing. Since 2003, he has been Director of the Signal Theory and Communications Department, UPC. He has published more than 150 papers on microwave tomography, radar, ISAR and SAR systems, SAR processing, and interferometry.

Jordi Romeu (Member, IEEE) was born in Barcelona, Spain, in 1962. He received the Ingeniero de Telecomunicación and Doctor Ingeniero de Telecomunicación degrees from the Universitat Politècnica de Catalunya (UPC), Barcelona, in 1986 and 1991, respectively.

In 1985, he joined the Photonic and Electromagnetic Engineering Group, Signal Theory and Communications Department, UPC. Currently he is a full Professor there, where he is engaged in research in antenna near-field measurements, antenna diagnostics, and antenna design. He was a Visiting Scholar with the Antenna Laboratory, University of California, Los Angeles, in 1999, on a NATO Scientific Program Scholarship, and in 2004 at the University of California Irvine. He has received several patents and has published 35 refereed papers in international journals and 50 conference proceedings.

Dr. Romeu was Grand Winner of the European IT Prize from by the European Commission for his contributions in the development of fractal antennas in 1998.

Sebastián Blanch (Member, IEEE) was born in Barcelona, Spain, in 1961. He received the Ingeniero and Doctor Ingeniero degrees in telecommunication engineering from the Universitat Politècnica de Catalunya (UPC), Barcelona, Spain, in 1989 and 1996, respectively.

In 1989, he joined the Electromagnetic and Photonics Engineering Group, Department of Signal Theory and Communications, UPC, where he is currently an Associate Professor. His research interests include near-field antenna measurements and imaging, antenna diagnostics, and antenna design.

Anna Papió Toda was born in Reus, Spain, in 1984. She is pursuing telecommunication engineering studies and computer sciences at the Universitat Politècnica de Catalunya (UPC), Barcelona, Spain.

Since February 2006, she has been a Research Assistant with the Department of Signal Theory and Communications, UPC, working on the topic of UWB imaging and location systems. During July–August 2006, she was a Visiting Researcher with the Institut für Höchstfrequenztechnik und Elektronik, Universität Karlsruhe, Germany, where she worked on UWB antenna characterization by means of FDTD simulations. In 2008, she has been performing a technical stay with Broadcom, Irvine, CA. Her research interests include antennas, electromagnetic scattering and imaging, and wireless systems.

Xavier Fàbregas (Member, IEEE) received the B.S. degree in physics from Barcelona University, Barcelona, Spain, in 1988 and the Ph.D. degree in applied sciences from the Universitat Politècnica de Catalunya (UPC), Barcelona, in 1995.

Since 1996, he has been an Associate Professor with UPC. In 2001, he spent an eight-month sabbatical with the HR Institute of the German Aerospace Agency, Oberpfaffenhofen. His current research interests include radar polarimetry, polarimetric-retrieval algorithms, and polarimetric calibration.

Angel Cardama (Member, IEEE) was born in Santiago de Compostela, Spain, in 1944. He received the Ingeniero de Telecomunicación degree from the Universidad Politécnica de Madrid, Spain, and the Sc.M. and Ph.D. degrees in electrical engineering from Brown University, Providence, RI, in 1968, 1970, and 1973, respectively.

In 1972, he joined the Faculty of the Telecommunication Engineering School, Universitat Politècnica de Catalunya (UPC), Barcelona, Spain, where he is a Professor. His research interests range from the development of analytical and numerical techniques in electromagnetics to the design of microwave imaging systems and radar and communications antennas.